PHOTOGRAMMETRIC RECONSTRUCTION USING A MFDC: SYSTEM CALIBRATION PERSPECTIVE

Ayman Habib, Ana Paula Kersting, Changjae Kim, Eunju Kwak, Yousif Alghamdi
Dept. of Geomatics Engineering, University of Calgary, 2500 University Dr. NW,
Calgary, Alberta, T2N 1N4, Canada.
ahabib@ucalgary.ca
ana.kersting@ucalgary.ca
cjkim@ucalgary.ca
ekwak@ucalgary.ca
yousif.ghamdi.12@aramco.com

ABSTRACT

Current advances in digital and electronic products have led to the availability of inexpensive and reliable Medium Format Digital Cameras (MFDCs) that can be used in many photogrammetric applications. In this research, the impact of camera and system mounting parameters calibration on object space reconstruction is investigated under different georeferencing scenarios (i.e., indirect georeferencing and integrated sensor orientation). First, camera calibration is conducted using a MFDC (i.e., the Rollei-P65). Based on different camera calibration datasets – such as indoor, in-situ, and camera calibration certificates, the equivalency of the calibration techniques as well as the adequacy of the distortion models are evaluated while considering relative and absolute quantitative measures. Previously developed camera stability analysis techniques are used for testing the adequacy of the utilized distortion model as well as the equivalency of different calibration techniques. Afterwards, system mounting parameters calibration is conducted to estimate the lever-arm and boresight parameters using different calibration datasets. The mounting parameters are estimated through an integrated sensor orientation (i.e., GPS/INS-assisted Aerial Triangulation) using minimum amount of control information. The estimated system calibration parameters are evaluated by investigating both relative and absolute quantitative measures using different camera calibration parameters. The experimental results have shown that the indoor calibration provides reliable estimate of the internal camera characteristics and leads to accurate system calibration and object space reconstruction.

INTRODUCTION

Photogrammetry focuses on accurate derivation of spatial and descriptive information from imagery to satisfy the needs of several applications. Accurate 3D reconstruction requires careful calibration of the photogrammetric system. Traditionally, object space reconstruction has been obtained through an indirect georeferencing procedure, where the image georeferencing parameters and the coordinates of the ground points are determined in a bundle adjustment procedure using corresponding tie points between images and ground control points. Point positioning derived through a traditional indirect georeferencing approach is illustrated in Figure 1. As demonstrated in this figure, the position of an object point $\vec{X}_G$ can be expressed by the summation of two vectors: $\vec{X}_o$ and $\vec{v}$ after applying the rotation $R_{\omega,\phi,\kappa}$ and the scale factor S as presented in Equation 1. In this equation, $\vec{X}_o$ represents the vector from the origin of the ground coordinate system to the camera perspective center and $R_{\omega,\phi,\kappa}$ the rotation matrix relating the ground and image coordinate systems. These terms ($\vec{X}_o$ and $R_{\omega,\phi,\kappa}$) are the exterior orientation parameters (EOP) of the exposure station, which are determined in the bundle adjustment procedure together with the ground coordinates of the tie points. The term $\vec{v}$ represents the vector from the perspective center to the image point $(x - x_p - dist_x, y - y_p - dist_y, -c)$ with respect to the image coordinate system. The magnitude of the vector $\vec{v}$, after applying the scale factor S, corresponds to the distance from the camera perspective center to the object point. The scale factor S can be determined through the intersection procedure if two or more images are available in the bundle adjustment procedure. The terms (x, y) represent the image coordinates while $(x_p, y_p, c, dist_x, dist_y)$ are the interior orientation parameters (IOP) of the camera (principal point coordinates, principal distance and distortion

parameters, respectively), which are determined in the camera calibration procedure. Therefore, in a traditional indirect georeferencing procedure the photogrammetric system calibration involves only the camera calibration procedure.

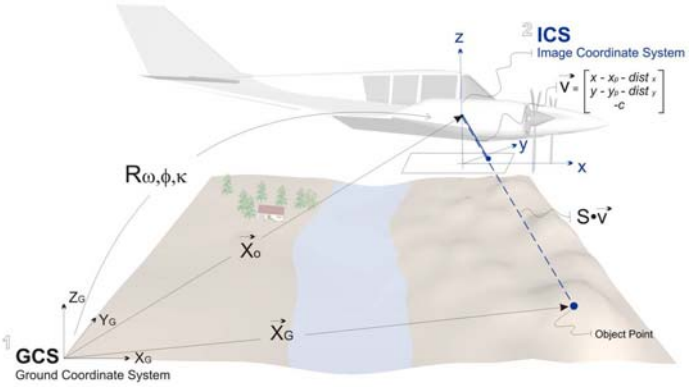

Figure 1. Point positioning equation of an indirect georeferencing procedure.

$$\vec{X}_G = \vec{X}_o + S\,R_{\omega\phi\kappa}\,\vec{v} = \vec{X}_o + S\,R_{\omega\phi\kappa}\begin{bmatrix} x - x_p - dist_x \\ y - y_p - dist_y \\ -c \end{bmatrix} \tag{1}$$

The availability of high accuracy positioning and orientation information obtained from the integration of GPS and INS systems has made it possible to perform direct image orientation without the need for ground control points. The object space reconstruction through direct sensor orientation is illustrated in Figure 2. As shown in this figure and presented in Equation 2, in the direct sensor orientation the position of the object point, $\vec{X}_G$, is derived through the summation of three vectors ($\vec{X}_o$, $\vec{P}_G$, and $\vec{v}$) after applying the appropriate rotations: $R_{yaw,\ pitch,\ roll}$ and $R_{\Delta\omega,\Delta\phi,\Delta\kappa}$, and scale factor S. In this equation, $\vec{X}_o$ is the vector from the origin of the ground coordinate system to the origin of the IMU coordinate system. This vector is derived from the GPS/INS integration procedure while considering the lever-arm offsets between the phase center of the GPS antenna and the IMU body frame. The term $\vec{P}_G$ is the offset between the camera perspective center and IMU coordinate systems (lever-arm offsets), while $R_{yaw,\ pitch,\ roll}$ stands for the rotation matrix relating the ground and IMU coordinate systems (derived through the GPS/INS integration process) and $R_{\Delta\omega,\Delta\phi,\Delta\kappa}$ represents the rotation matrix relating the IMU and camera frame coordinate systems (defined by the boresight angles). The boresight angles and lever-arm offsets are determined in the system mounting parameter calibration procedure. In contrast to indirect georeferencing, where only the camera calibration is needed, direct sensor orientation involves besides the camera calibration the system mounting parameters calibration. Moreover, camera calibration plays a more important role in the direct sensor orientation than in the indirect sensor orientation. This is mainly due to the fact that direct sensor orientation is an extrapolation procedure and errors are directly propagated to the object space (Habib and Shenk, 2001). For instance, errors in the calibration parameters cannot be compensated by the exterior orientation parameters. Therefore, reliable camera and system mounting parameters calibration are essential to obtain accurate object space reconstruction.

In the camera calibration procedure, the internal characteristics of a camera, which are defined by its IOP, are determined. In the system mounting parameters calibration, on the other hand, the lever-arm offsets and boresight angles relating the photogrammetric system components, such as the camera, the GPS and INS systems are determined. Direct sensor orientation can be subdivided into (i) Integrated Sensor Orientation and (ii) Direct georeferencing (Jacobsen, 2004). The Integrated Sensor Orientation can be performed in the two following ways: (a) GPS-assisted aerial triangulation: where only GPS positions are available and the attitude parameters are determined in the bundle adjustment procedure, (b) GPS/INS-assisted aerial triangulation: where GPS and INS position and attitude information are available and used as prior information in the bundle adjustment procedure. In the Direct georeferencing, GPS and INS position and attitude information are available and used together with the

image coordinates of tie points in a simple intersection procedure.

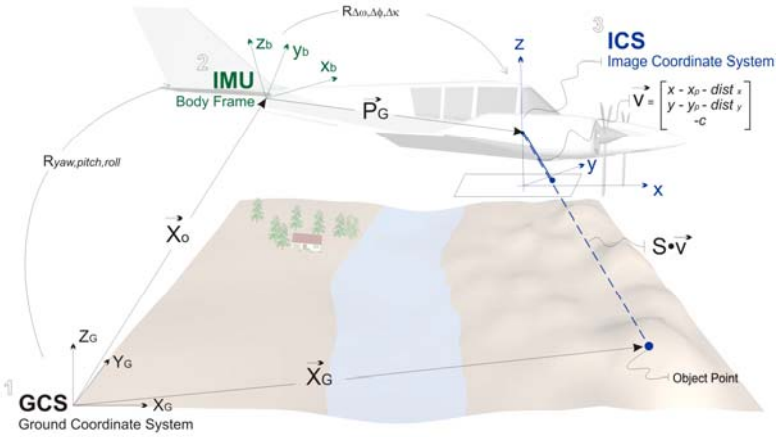

Figure 2. Point positioning equation of a direct sensor orientation procedure.

$$\vec{X}_G = \vec{X}_o + R_{yaw,\ pitch,\ roll}\ \vec{P}_G + SR_{yaw,\ pitch,\ roll}\ R_{\Delta\omega,\Delta\phi,\Delta\kappa}\begin{bmatrix} x - x_p - dist_x \\ y - y_p - dist_y \\ -c \end{bmatrix} \tag{2}$$

The camera interior orientation parameters include the principal distance, the coordinates of the principal point, and the distortion model parameters. A distortion model is the mathematical representation of the corrections that compensate for various deviations from the assumed collinearity condition. There exist several variations of distortion models that can be used to model inherent distortions such as the Brown-Conrady model (Brown, 1966; Brown 1971), the USGS Simultaneous Multi-frame Analytical Calibration (SMAC) model (USGS, 2008), and the Orthogonal polynomials model (Ebner, 1976; Grün, 1978). In Habib et al. (2008), the equivalency between some of these distortion models has already been tested. In this research work, the Brown-Conrady distortion model is utilized (Equation 3).

$$\begin{aligned} dist_x &= K_1(r^2 - R_o^2)\bar{x} + K_2(r^4 - R_o^4)\bar{x} + P_1(r^2 + 2\bar{x}^2) + 2P_2\bar{x}\bar{y} - A_1\bar{x} + A_2\bar{y} \\ dist_y &= K_1(r^2 - R_o^2)\bar{y} + K_2(r^4 - R_o^4)\bar{y} + P_2(r^2 + 2\bar{y}^2) + 2P_1\bar{x}\bar{y} + A_1\bar{y} \end{aligned} \tag{3}$$

where:

- x_p and y_p are the image coordinates of the principal point,
- $\bar{x} = x - x_p$ and $\bar{y} = y - y_p$ are the image coordinates reduced to the principal point,
- $r = \sqrt{(x - x_p)^2 + (y - y_p)^2}$ is the radial distance between the point in question and the principal point,
- K_1 and K_2 are the radial lens distortion parameters,
- R_o is a camera-specific constant,
- P_1 and P_2 are the de-centric lens distortion parameters,
- A_1 and A_2 are the affine deformation parameters.

Traditionally, large format analogue cameras have been used in photogrammetric activities. In the last few years, however, digital cameras are becoming more common in photogrammetric activities and are rapidly replacing the need for the conventional large format analogue cameras. This trend can be explained by the ease of use, decreasing cost, and increasing resolution of digital cameras. The airborne digital cameras that are currently available can be grouped into two main categories: the first group includes large format digital cameras, such as line cameras (e.g., ADS50 from Leica Geosystems) and large format frame cameras (e.g., DMC^{TM} from Zeiss/Intergraph); while the second group includes medium to small-format digital cameras (e.g., Rollei-P65). For large format analogue cameras, the well defined laboratory calibration process is executed. The laboratory calibration is usually performed by system manufacturers and dedicated organizations (such as the USGS, NRCan), where trained professionals ensure that high calibration quality is upheld. In contrast to the standard analogue cameras, the calibration process for digital cameras is a more complex task. The difficulty is attributed to the large variety of camera designs available in the market, which would demand different facilities and calibration

approaches (Cramer, 2004). This is not critical for large format digital cameras that are specifically built for mapping applications. For these cameras, the calibration process is conducted by the system manufacturer (e.g., Leica or Z/I). This is not the case for MFDCs, which are not manufactured for photogrammetric purposes and have been increasingly used in photogrammetric activities. The increased use of MFDCs by the photogrammetric community is noticeable, especially in conjunction with LiDAR systems and in smaller coverage flight blocks. The preference given by some data providers to MFDCs is attributed to its lower cost when compared with large format digital cameras. The wide spectrum of existing designs for MFDCs coupled with the large number of this type of camera in use by the photogrammetric community make it impracticable for the system manufacturer and/or few specialized organizations to execute the laboratory calibration. In addition, the stability of MFDCs is also a concern, given the fact that these cameras are not manufactured for photogrammetric purposes. Therefore, it has become more practical for the data providers to perform their own calibrations and stability analysis of the utilized cameras. In this context, more attention should be placed towards the method and quality of the camera calibration. More specifically, the appropriate calibration procedure and stability analysis as well as the adequate model to represent the inherent distortions in the implemented camera should be carefully investigated.

As already mentioned, in direct sensor orientation, besides the camera calibration, the system mounting parameters calibration is also needed and is crucial for obtaining an accurate object space reconstruction. The method for the estimation of the system mounting parameters can be carried out through a two-step or a single-step procedure. In the two-step procedure, the system mounting parameters are estimated by comparing the GPS/INS positioning and orientation results with the exterior orientation parameters determined from an independent aerotriangulation solution. As an example, in Skaloud (1999) the mounting parameters are estimated for each image separately and then the results undergo an average weighting procedure. In the single-step procedure, on the other hand, the mounting parameters are estimated in the bundle adjustment procedure. There are two approaches for the single-step procedure. In the first approach, existing bundle adjustment procedures are extended with added constraints (Grejner-Brzezinska, 1999), while in the second approach, GPS/INS measurements and the system mounting parameters are directly incorporated in the collinearity equations (Pinto and Forlani, 2002).

In this paper, the MFDC Rollei-P65 is investigated. Using this camera, the distortion model adequacy will be evaluated and the equivalency of camera calibration techniques/datasets, such as the indoor and the in-situ, will also be tested. In addition, system calibration will be conducted through an integrated sensor orientation to estimate the lever-arm and boresight parameters (i.e., mounting parameters) using different calibration datasets. The single-step procedure that extends the existing bundle adjustment procedure with additional constraints will be utilized. This paper starts by presenting the methodology that will be used to test the adequacy of the distortion models and the equivalency of the calibration datasets. Then, the aspects involved in the design and implementation of an in-flight mounting parameters calibration, as they relate to control and flight configuration requirements, are investigated. Finally, experimental results using real data are presented followed by conclusions and recommendations for future work.

ADEQUACY OF DISTORTION MODELS AND EQUIVALENCY OF CALIBRATION DATASETS

In this section, the methodology for evaluating the distortion model adequacy and for testing the equivalency of the calibration techniques/datasets is introduced. A model can be classified as being one of three categories: inadequate, adequate, or over-parameterized. An adequate model has the minimum number of distortion parameters needed to sufficiently describe the inherent distortions in the implemented camera. Insufficient and over-parameterized distortion models should be avoided since they will have an adverse effect on the system mounting parameters calibration as well as on the reconstructed object space. The adequacy of a model with a set of parameters can be carried out by adding one parameter at a time until the minimum number of parameters that is capable of properly representing the phenomenon under investigation is determined. In this work, the adequacy of the distortion model is evaluated by incrementally increasing the model parameters while checking:

(1) The outcome of the bundle adjustment with self calibration procedure: A reduction in the a-posteriori variance factor indicates a transition from an insufficient distortion model to a better one. On the other hand, insignificant change in the a-posteriori variance factor indicates a transition from an adequate distortion model to an over-parameterized one. In terms of the accuracy of the estimated distortion parameters, poor accuracy

should be expected for insufficient and over-parameterized models. In addition, higher correlations among the elements of the IOP and EOP are expected for over-parameterized models.

(2) Analysis of the bundle similarity: The bundles defined by each of the distortion models will be checked for similarity. For that purpose, bundle similarity methods previously used for camera stability analysis will be employed (Habib et al., 2006). Three bundle similarity methods will be utilized in this work: the ZROT (Zero Rotation), ROT (Rotation) and SPR (Single Photo Resection) methods. The ZROT and ROT procedures evaluate the similarity between the shapes of the defined bundles. The main difference is that the ZROT procedure evaluates the degree of similarity between the defined bundles while sharing the same position and orientation in space. The ROT procedure, on the other hand, evaluates the similarity of the bundles while sharing only the same position in space. In other words, the ROT procedure allows for relative rotations between the two bundles to assure the best similarity possible. The SPR procedure does not evaluate the degree of similarity between the shapes of the involved bundles. It just evaluates the quality of fit between these bundles at a given object space (for specific flight height and terrain height variation). In the SPR procedures, the bundles are allowed to freely shift and rotate in space to assure the best fit at the given object space. To evaluate the degree of similarity between two defined bundles, a similarity measure ($RMSE_{offset}$) value is computed. The $RMSE_{offset}$ is a global measure that describes the average offset along the image plane between conjugate light rays in two bundles, which are derived from two IOP sets (Figure 3). The two bundles are deemed similar if the computed $RMSE_{offset}$ is within the range defined by the expected standard deviation of the image coordinate measurements (i.e., 1/2 pixel). For details on how the $RMSE_{offset}$ is computed in each of the bundle similarity methods, interested readers can refer to Habib et al. (2006) and Habib et al. (2008). The adequacy of the distortion model using the bundle similarity methods will be checked as follows:

a. The transition from insufficient to adequate models should be manifested in a change in the shape of the reconstructed bundles.
b. The transition from adequate to over-parameterized models should be manifested in having bundles with similar shapes.

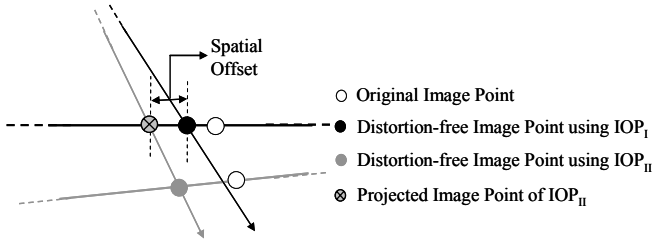

Figure 3. Illustration of how the $RMSE_{offset}$ is computed in the image space between two bundles defined by two different calibration datasets.

(3) Verification of the adequate model through photogrammetric reconstruction using different georeferencing procedures: the adequate model according to 1) and 2) will be verified/confirmed by analyzing the outcome (i.e., a-posteriori variance factor $(\hat{\sigma}_o)^2$ and RMSE – check point analysis) of the indirect georeferencing and GPS/INS-assisted aerial triangulation procedures. In addition, the validity of the estimated lever-arm components, i.e., the proximity of the physically measured lever-arm parameters to the estimated ones through the GPS/INS-assisted aerial triangulation will be verified as well.

So far, the methodology for evaluating the distortion model adequacy has been described. Now, the methodology for testing the equivalency of calibration datasets is presented. In this paper, we would like to test the equivalency of the calibration datasets from the camera calibration certificate, indoor and in-situ calibrations. Similar to the methodology for checking the distortion model adequacy, the bundle similarity methods will be utilized to check the equivalency of the calibration datasets, as in (2). More specifically, if two bundles defined using the calibration parameters estimated using two different calibration techniques are deemed similar (i.e., $RMSE_{offset}$ < ½ pixel), then these two calibration techniques/datasets are deemed equivalent. The equivalency of the calibration procedures are then verified through photogrammetric reconstruction using different georeferencing procedures, as in (3).

To investigate the optimum flight configuration and the minimum ground control requirement, the impact of biases in the system mounting parameters on the derived object space will be analyzed through mathematical analysis of the direct sensor orientation point positioning equation (Equation 2). It should be noted that point reconstruction from overlapping imagery is only possible if conjugate light rays intersect. In the presence of biases in the system mounting parameters, intersection will occur only if these biases do not introduce artificial Y-parallax (assuming flight direction parallel to the X axis). Therefore, an appropriate analysis of the impact of the biases on the object space should verify whether an artificial Y-parallax is introduced in the presence of such biases. If an artificial Y-parallax is introduced by a specific bias, then such a bias can be recovered using a control-free stereo-pair. In other words, the introduced artificial Y-parallax provides a constraint allowing for the recovery of such a bias. The concept of the proposed mathematical analysis is outlined in the next paragraphs.

In order to investigate whether biases in the system mounting parameters will introduce artificial Y-parallax, we can generate a pair of normalized images from the stereo-pair under consideration. More specifically, an image pair which is parallel to the XY-plane of the IMU body frame (considering that the baseline is parallel to the X-axis of the IMU body frame) can be generated. In the normalized image pair no Y-parallax exists. To analyze the impact of the biases in the mounting parameters on the normalized image plane, we can differentiate the equations that express the normalized coordinates in terms of the mounting parameters. The outcome of such analysis, after ignoring higher order terms, corresponds to the displacements in the normalized image coordinates caused by each of the mounting parameters biases. Based on these derived displacements, it is possible to verify whether or not these displacements will introduce artificial Y-parallax. One can note that biases in the $\Delta\phi$ (boresight pitch angle) and $\Delta\kappa$ (boresight yaw angle) will introduce artificial Y-parallax. These findings reveal the possibility of estimating biases in the boresight pitch and yaw angles using a control-free stereo pair.

To evaluate the impact of the mounting parameters biases on the reconstructed object space, one can introduce the displacements caused by each of these biases to the normalized coordinates from the left and right images. Using such coordinates from the left and right normalized images, the biased object space coordinates can be derived. By performing such analysis, one can conclude the following:

- The boresight pitch bias will cause a non-linear shift along the flight direction and a smaller non-linear shift in the across flight direction. The boresight pitch bias will also cause a shift in the Z direction with its magnitude varying linearly along the flying direction. All these effects are dependent on the flying height and direction. The planimetric effect along the flight direction and the vertical effect are dependent on the x image coordinate. The planimetric effect across the flight direction, on the other hand, is dependent on the x and y image coordinates.
- The boresight yaw bias will cause a shift along the flying direction with its magnitude varying linearly across the flight direction. This effect is dependent on the flying height and the y image coordinate. The boresight yaw bias will also cause a shift across the flying direction with its magnitude varying linearly along the flight direction. This effect is dependent on the flying height and the x image coordinate. Both effects are independent of the flying direction. This effect is equivalent to a shearing effect in the X and Y directions (the surface will be distorted).
- The boresight roll bias will cause a constant shift across the flight direction and a shift in the Z direction with its magnitude varying linearly across the flying direction (it will tilt the surface in the across flight direction). Both effects are dependent on the flying height and direction. The planimetric effect across the flight direction is independent of the image point coordinates (x, y). The vertical effect, on the other hand, is dependent on the y image coordinate (the image coordinates in the across flight direction).
- The biases in the lever-arm offset will lead to constant shifts in the derived point cloud. The shifts in the XY-directions are dependent on the flying direction. The shift in the Z-direction, on the other hand, is independent of the flying direction. The planimetric and vertical shifts are independent of the flying height and the image point coordinates (x, y).

Based on the impact of the biases in the mounting parameters on the derived object space listed above, one can devise the optimum flight configuration that maximizes the impact of biases in the mounting parameters. The impact of the pitch and the yaw bias in the object space reveals the possibility of estimating these parameters from a single flight line, or even a single stereo image pair since an artificial Y-parallax is introduced in the object space. However, having opposite flight lines with almost 100% side lap allows for a better estimate of the boresight pitch angle bias, as well as the boresight roll and the planimetric lever-arm offsets biases. Having parallel flight lines with

the least overlap possible (e.g., 30 – 50%) would allow for a more reliable estimate of the boresight yaw angle. Note that only a vertical bias in the lever-arm offset parameters cannot be detected by observing discrepancies between conjugate surface elements in adjacent flight strips. Such inability is caused by the fact that a vertical bias in the lever-arm offset parameters produces the same effect regardless of the flying direction, flying height, or image point coordinates. Therefore, at least one vertical ground control point would be required to estimate the vertical component of the lever-arm offset vector. Figure 4 illustrates the devised optimum flight and control configuration for the estimation of the system mounting parameters.

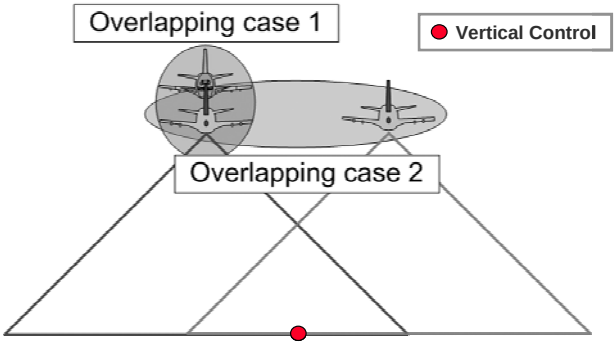

Figure 4. Optimum flight and control configuration for the estimation of the system mounting parameters.

EXPERIMENTAL RESULTS

In this section, experiments with real data are carried out to investigate the distortion model adequacy and the equivalency of calibration datasets. In addition, the minimum control and flight configuration requirements for the system mounting parameters calibration will be verified. Moreover, it will be checked whether the given a-priori accuracies for the GPS/INS position and orientation information are realistic.

The dataset tested in this research work was acquired by a MFDC Rollei P-65. The utilized camera has an array dimension of 8984x6732 pixels and a focal length of 60 mm. A total of eighteen convergent images were taken for the indoor camera calibration experiment. The GPS/INS-assisted flight mission configuration consists of a total of six flight lines acquired in two flight dates, where four flight lines were flown in the E-W direction and two flight lines in the N-S direction, (in opposite directions) with 60% overlap. The flight lines flown in the E-W direction were acquired from a flying height of ~550 m (above MSL) and 80% side lap. The flight lines flown in the N-S direction were obtained from a flying height of ~1200 m (above MSL) and 100% side lap. The given GPS and INS accuracy by the data provider is ±10 cm and ±10 sec, respectively. In the surveyed area, thirty-seven control points were established. These control points were used for the in-situ calibration and for check point analysis. Although this dataset was not acquired for use in an in-situ calibration, which would require significant terrain height variation and/or oblique imagery, it was used for that purpose.

The indoor and the in-situ camera calibration were performed using bundle adjustment with self-calibration under an indirect georeferencing procedure. Three different distortion models are investigated in this paper. The first model, denoted in this paper as *A*, includes K_1 only. The second model is denoted as *B* and includes the parameters K_1 and K_2. Finally, the third model, denoted as *C*, includes the parameters K_1, K_2, P_1, P_2, A_1, and A_2 (refer to equation 3). Table 1 reports the calibration results for the indoor and in-situ techniques using the three different distortion models. In the in-situ calibration, for all three distortion models, correlations between c and Z_o, and Z_o among images were found to be higher than 0.99. As mentioned earlier, the utilized test field was not designed for an in-situ calibration. More specifically, the utilized test field is relatively flat (i.e., no significant height variation). Furthermore, almost vertical images were taken instead of oblique images and therefore, c and Z_o could not be decoupled. The correlations between these parameters significantly reduce the reliability of the IOP acquired by this in-situ camera calibration. This is also expressed by the higher standard deviation of the estimated parameters when compared to the indoor cases. Therefore, only the indoor calibration will be considered for testing the adequacy of the distortion models.

It can be noticed in Table 1 that there is a significant improvement in the a-posteriori variance factor $(\hat{\sigma}_o)^2$ when utilizing the distortion model *B* instead of model *A*. In other words, model *B* leads to a better fit between the

observations and the estimated parameters, including the IOP, more than that resulting from model *A*. The same significant improvement can be observed in the standard deviations of the estimated parameters in model *A* and *B*. The improvement in the a-posteriori variance factor $(\hat{\sigma}_o)^2$, on the other hand, is less significant when using the distortion model *C* instead of model *B*. A closer look at the indoor results also reveals that even though the a-posteriori variance factor $(\hat{\sigma}_o)^2$ of model *C* is slightly better than that in model *B*, the standard deviation of some of the estimated parameters (e.g., x_p, y_p) using model *B* is better than that in model *C*. This can be explained by the over-parameterization in model *C* that leads to correlation among the IOP and among the IOP and EOP. The correlation within the IOP is mainly between the x_p, y_p and P_1, P_2 (note the significant deviations between the estimates of x_p, y_p in models *B* and *C*). As a result, model *B* leads to better estimate of the IOP when compared with model *C*. Based on these results, we can conclude that model *A* is an **inadequate** model and model *B* is an **adequate** model for representing the inherent distortions in the implemented camera. Therefore, differently from what is usually assumed for MFDCs, K_1 is not sufficient to model the lens distortion of the MFDC used in this research work. Model C, on the other hand, is an **over-parameterized** model that leads to correlation among the elements of the IOP as well as correlation between the IOP and EOP.

Now, it will be verified whether we can use the bundle similarity approach to prove the adequacy of model *B*. For that purpose, distortion model adequacy was verified for the three different models according to the ZROT, ROT and SPR bundle similarity methods. The results are presented in Table 2. One can observe in the reported $RMSE_{offset}$ values in Table 2 that models *A* and *B* define two different bundles regardless of the utilized similarity model ($RMSE_{offset}$ larger than 1/2 pixel for all methods). Models *B* and *C*, on the other hand, are deemed similar according to the ROT and SPR methods and deemed different according to the ZROT method. The non-similarity between models *B* and *C* according to ZROT can be explained by the over-parameterization introduced by model *C* which leads to some correlation among the IOP as well as among the IOP and the EOP while keeping the same shape of the bundles defined by model *B*. In other words, models *B* and *C* produce bundles with similar shape, i.e., the bundles are in agreement with each other after applying some rotations, and therefore are similar according to ROT and SPR methods. Therefore, model *C* does not lead to variation in the shape of the bundle when compared with model *B*. These results confirm the adequacy of the model *B* to represent the distortions inherent in the implemented camera.

So far, the focus has been on the analysis of the distortion model adequacy. Now, the bundle similarity approaches will be used to check the equivalence of the calibration parameters from the indoor and from the CCC. Table 3 reports the equivalency results using the ZROT, ROT, and SPR methods. Note that, in the comparative analysis only model *B* is used in all calibration techniques as it has already been proven that this is the adequate model. We can observe in Table 3 that the indoor and the CCC calibration parameters are deemed similar according to all methods except the ZROT procedure.

Now, the impact of the utilized distortion model and the equivalency of the calibration procedures/datasets on the indirect georeferencing procedure will be verified. Table 4 presents the indirect georeferencing results (estimated a-posteriori variance factor and the RMSE – check point analysis) using various calibration datasets. It can be noted in the reported values in this table that the inadequacy of model *A* in describing the inherent distortions in the involved camera is manifested in the worst a-posteriori variance factor among the tested models. As expected, the $(\hat{\sigma}_o)^2$ and the RMSE for the indoor models *A* and *B* are quite different given that these two models were deemed different regardless of the utilized method (SPR, ROT, ZROT). On the other hand, similar $(\hat{\sigma}_o)^2$ and RMSE values for the indoor models *B* and *C* can be observed. This similarity is expected since these two models were deemed similar according to the ROT and SPR methods, thus confirming the adequacy of the model *B*.

Table 5 presents the estimated a-posteriori variance factor, lever-arm components, and RMSE values (check point analysis) using GPS-Assisted aerial triangulation using different IOP sets. As in the indirect georeferencing case, the inadequacy of model *A* in describing the inherent distortions in the involved camera is manifested in the worst a-posteriori variance factor among the tested models. Moreover, the inadequacy of model *A* results in unrealistic estimate of the lever-arm components when compared with the physically measured ones. The indoor calibration (model *B*) leads to the closest estimate of the lever arm components when compared to the physically measured ones. It also leads to the best RMSE results when compared with the other tested models (highlighted cells in Table 5). On the other hand, the over-parameterized model *C* leads to unrealistic estimate of the lever-arm components as well as worse estimate of the RMSE values when compared with the outcome from the indoor calibration (model *B*), Table 5. In terms of equivalency of the calibration procedures, it can be observed in Table 5 that, in spite of the fact that the indoor and the CCC have almost equivalent RMSE values, the later produces less

realistic estimates of the lever-arm components. Therefore, the indoor calibration produces the most faithful description of the inherent distortions in the involved camera. Another conclusion that can be drawn from the experiments reported in Table 5 is that the estimated lever-arm components for a given distortion model do not significantly change with the increase in the number of utilized GCP. Hence, one can conclude that a single vertical GCP is sufficient for the estimation of the lever-arm components for an optimal flight configuration.

Table 6 reports the GPS residuals, i.e., the difference between the adjusted GPS positions and the observed ones. These residuals are expected to have the same standard deviation of the given a-priori accuracy. The reported residuals in Table 6 verify that the a-priori accuracy of the available positions of the exposure stations (±10cm) is realistic if not conservative.

Table 7 presents the GPS/INS-assisted aerial triangulation results using different calibration datasets for the estimation of the system mounting parameters. As in the indirect georeferencing and GPS-assisted triangulation cases, it can be observed in the reported values that model *A* leads to the worst a-posteriori variance factor among the tested models, verifying its inadequacy for representing the inherent distortions in the involved camera. Here again, model *B* leads to one of the best a-posteriori variance factors, proving the adequacy of this model in representing the inherent distortions in the implemented camera. However, the estimated a-posteriori variance factor using GPS/INS integrated sensor orientation and the given a-priori standard deviations of ±10cm and ±10sec (for the position and orientation information at the exposure stations, respectively) is worse than the estimated a-posteriori variance factor using GPS integrated sensor orientation and the given a–priori standard deviation of ±10cm (Table 7). Such deterioration can be attributed to an optimistic a-priori standard deviation of the available attitude (±10sec). The reported position and orientation residuals (Tables 8 and 9, respectively) indicate worse residuals when using ±10sec as a-priori standard deviation for the available attitude. Therefore, it is believed that ±100sec is a more realistic estimate of the a-priori standard deviation of the available attitude. A possible cause of the worse attitude accuracy is the fact that the data was collected in two different flight dates with inaccurate/incomplete INS drift modeling in the GPS/INS integration process. These findings explain the significant deviation of the estimated lever-arm parameters from the physically measured ones (compare the highlighted cells in Tables 5 and 7).

Table 10 shows the GPS/INS-assisted results using the deemed correct a-priori standard deviations of ±10cm and ±100sec (for the position and orientation information at the exposure stations, respectively). Note that the estimated a-posteriori variance factor using GPS/INS integrated sensor orientation with an a-priori standard deviation of ±10cm and ±100sec for the available position and orientation, respectively, is almost equivalent to the estimated a-posteriori variance factor using GPS integrated sensor orientation and the a-priori standard deviation of ±10cm. Such equivalency is an indication of the validity of the utilized a-priori standard deviation of the available attitude (±100sec). The validity of the utilized standard deviation of the available attitude led to estimates of the lever-arm components that are closer to the physically measured values (refer to the highlighted cells in Table 10). It is worth noting that the indoor calibration (model *B*) leads to the best reconstruction as evaluated by the RMSE values from the checkpoint analysis as well as estimates of the lever arm components that are closer to the physically measured values. Once again, increasing the number of implemented GCP does not lead to significant changes in the estimated mounting parameters. This indicates that a single vertical GCP is sufficient for the estimation of the mounting parameters given that an appropriate flight configuration was utilized.

Table 1. Calibration results using indoor and in-situ techniques and the distortion models under investigation.

	Indoor (*A*)	Indoor (*B*)	Indoor (*C*)	In-Situ (*A*)	In-Situ (*B*)	In-Situ (*C*)
$(\hat{\sigma}_o)^2$ (mm)^2	$(0.0019)^2$	$(0.0011)^2$	$(0.0010)^2$	$(0.0050)^2$	$(0.0020)^2$	$(0.0017)^2$
x_p (mm±mm)	0.0653 ±0.0050	0.0649 ±0.0028	0.0058 ±0.0069	0.0501 ±0.0406	0.0921 ±0.0167	-0.0029 ±0.0164
y_p (mm±mm)	0.1484 ±0.0049	0.1541 ±0.0027	0.0829 ±0.0069	0.1843 ±0.0413	0.1751 ±0.0170	0.1012 ±0.0164
c (mm±mm)	60.686 ±0.0123	60.678 ±0.0070	60.681 ±0.0065	60.713 ±0.3887	60.783 ±0.1598	60.672 ±0.1376
K_1 (mm^{-2}± mm^{-2})	-2.0137e-007 ±7.5957e-008	-4.2737e-006 ±9.5110e-008	-4.2090e-006 ±9.1696e-008	1.8516e-006 ±1.3248e-007	-3.9882e-006 ±1.1422e-007	-4.0168e-006 ±9.7047e-008
K_2 (mm^{-4}± mm^{-4})	-	5.5041e-009 ±1.1476e-010	5.4768e-009 ±1.0631e-010	-	5.4293e-009 ±9.3405e-011	5.4038e-009 ±7.9654e-011
P_1 (mm^{-1}± mm^{-1})	-	-	-5.4675e-006 ±6.0061e-007	-	-	-5.5541e-006 ±4.9130e-007
P_2 (mm^{-1}± mm^{-1})	-	-	-6.5251e-006 ±6.0055e-007	-	-	7.0255e-006 ±6.0257e-007
A_1	-	-	1.1723e-005 ±5.5275e-006	-	-	-1.7625e-006 ±9.7739e-006
A_2	-	-	-3.0024e-005 ±9.0786e-006	-	-	-6.5324e-005 ±1.7521e-005

Table 2. Adequacy of the distortion models using the indoor calibration technique.

	ZROT – $RMSE_{offset}$ (mm)	ROT - $RMSE_{offset}$ (mm)	SPR – $RMSE_{offset}$ (mm)
Indoor (*A*) vs. Indoor (*B*)	0.009714 (1.619 pixel)	0.008798 (1.466 pixel)	0.003611 (0.602 pixel)
Indoor (*B*) vs. Indoor (*C*)	0.069173 (11.529 pixel)	0.001506 (0.251 pixel)	0.001205 (0.200 pixel)

Table 3. Equivalency of the indoor and CCC calibration datasets.

	ZROT - $RMSE_{offset}$ (mm)	ROT - $RMSE_{offset}$ (mm)	SPR – $RMSE_{offset}$ (mm)
Indoor (*B*) vs. CCC (*B*)	0.021186 (3.531 pixel)	0.001430 (0.238 pixel)	0.000981 (0.164 pixel)

Table 4. Indirect georeferencing results using different calibration datasets using ten ground control points and twenty-seven check points.

	$(\hat{\sigma}_o)^2$ (mm)^2	RMSE_X(m)	RMSE_Y(m)	RMSE_Z(m)
Indoor (*A*)	$(0.0060)^2$	0.071	0.096	0.596
Indoor (*B*)	$(0.0021)^2$	0.051	0.047	0.103
Indoor (*C*)	$(0.0025)^2$	0.081	0.064	0.083
CCC (*B*)	$(0.0022)^2$	0.054	0.051	0.165

Table 5. Estimated a-posteriori variance factor, lever-arm components, and RMSE values using GPS-Assisted aerotriangulation using different IOP sets (A-priori position accuracy ±10cm).

Camera Calibration Datasets + GCP	$\hat{\sigma}_o^2$ (mm)^2	Estimated Lever-Arm Parameters			RMSE_X (m)	RMSE_Y (m)	RMSE_Z (m)
		dx (m)	dy (m)	dz (m)			
Indoor (*A*) + 1 vertical GCP	$(0.0077)^2$	0.329	-0.139	0.353	0.283	0.292	0.218
Indoor (*B*) + 1 vertical GCP	$(0.0022)^2$	-0.087	-0.145	1.116	0.079	0.097	0.157
Indoor (*B*) + 37 vertical GCP	$(0.0021)^2$	-0.098	-0.153	1.148	0.100	0.081	N/A
Indoor (*B*) + 37 full GCP	$(0.0021)^2$	-0.066	-0.156	1.254	N/A	N/A	N/A
Indoor (*C*) + 1 vertical GCP	$(0.0030)^2$	0.259	-1.604	1.183	0.127	0.438	0.239
CCC (*B*) + 1 vertical GCP	$(0.0024)^2$	-0.171	-0.503	1.039	0.082	0.151	0.157
Physically measured values	-	-0.180	-0.170	1.065			

Table 6. Predicted position residuals from GPS-Assisted aerotriangulation using ±10cm as a-priori accuracy for the available position at the exposure stations while using the indoor calibration (model *B*), 1 Vertical GCP.

	GPS Residuals		
	X(m)	Y(m)	Z(m)
Mean	0.000	0.000	0.000
STD	0.038	0.043	0.056
RMSE	0.038	0.042	0.055

Table 7. Estimated a-posteriori variance factor, lever-arm components, and RMSE values using GPS/INS-Assisted aerotriangulatrion (±10cm & ±10sec) using different calibration datasets.

Camera Calibration Datasets + GCP	$\hat{\sigma}_o^2$ (mm)^2	Lever-Arms			Boresight angles			RMSE_X (m)	RMSE_Y (m)	RMSE_Z (m)
		dx (m)	dy (m)	dz (m)	dω (º)	dφ (°)	dκ (°)			
Indoor (*A*) + 1 vertical GCP	$(0.0090)^2$	0.586	-0.025	0.833	-0.1326	0.8966	179.5640	0.089	0.097	0.220
Indoor (*B*) + 1 vertical GCP	$(0.0054)^2$	0.250	-0.009	1.163	-0.1333	0.8800	179.5649	0.190	0.114	0.172
Indoor (*B*) + 37 vertical GCP	$(0.0051)^2$	0.192	-0.015	1.021	-0.1329	0.8762	179.5553	0.202	0.115	NA
Indoor (*B*) + 37 full GCP	$(0.0051)^2$	0.353	-0.050	1.143	-0.1322	0.8814	179.5647	NA	NA	NA
Indoor (*C*) + 1 vertical GCP	$(0.0059)^2$	0.505	-1.167	1.186	-0.1034	0.8324	179.5590	0.157	0.246	0.218
CCC (B) + 1 vertical GCP	$(0.0055)^2$	0.187	-0.297	1.168	-0.1397	0.8834	179.5639	0.207	0.110	0.184
Physically measured values	-	-0.180	-0.170	1.065	-	-	-			

Table 8. Predicted position residuals from GPS/INS-assisted aerotriangulation using different a-priori accuracy for the available position and orientation at the exposure stations while using the Indoor calibration (model *B*).

	GPS residuals											
	Indoor (*B*) + 1 Vertical GCP +GPS10cm+INS10sec			Indoor (*B*) + 1 Vertical GCP +GPS10cm+INS30sec			Indoor (*B*) + 1 Vertical GCP +GPS10cm+INS50sec			Indoor (*B*) + 1 Vertical GCP +GPS10cm+INS100sec		
	X(m)	Y(m)	Z(m)	X(m)	Y(m)	Z(m)	X(m)	Y(m)	Z(m)	X(m)	Y(m)	Z(m)
Mean	0.000	0.000	-0.003	0.000	0.000	-0.003	0.000	0.000	-0.002	0.000	0.000	-0.001
STD	0.482	0.374	0.190	0.332	0.242	0.141	0.215	0.158	0.099	0.094	0.078	0.062
RMSE	0.475	0.368	0.187	0.326	0.238	0.138	0.212	0.155	0.097	0.092	0.076	0.061

Table 9. Predicted attitude residuals from GPS/INS-assisted aerotriangulation using different a-priori accuracy for the available position and orientation at the exposure stations while using the Indoor calibration (model *B*).

	INS residuals											
	Indoor (*B*) + 1 Vertical GCP + GPS10cm+INS10sec			Indoor (*B*) + 1 Vertical GCP + GPS10cm+INS30sec			Indoor (*B*) + 1 Vertical GCP + GPS10cm+INS50sec			Indoor (*B*) + 1 Vertical GCP + GPS10cm+INS100sec		
	ω (sec)	φ (sec)	κ (sec)	ω (sec)	φ (sec)	κ (sec)	ω (sec)	φ (sec)	κ (sec)	ω (sec)	φ (sec)	κ (sec)
Mean	0	2	1	1	12	4	4	21	5	10	34	6
STD	11	13	16	56	67	39	88	110	51	122	157	67
RMSE	11	13	16	55	67	39	87	111	51	120	158	66

Table 10. Estimated a-posteriori variance factor, lever-arm components, and RMSE values using GPS/INS-Assisted Integrated Sensor Orientation (ISO – ±10cm & ±100sec) using different calibration datasets.

Camera Calibration Datasets + GCP	$\hat{\sigma}_o^2$ $(mm)^2$	Lever-Arms			Boresight angles			RMSE_X (m)	RMSE_Y (m)	RMSE_Z (m)
		dx (m)	dy (m)	dz (m)	dω (°)	dφ (°)	dκ (°)			
Indoor (A) + 1 vertical GCP	$(0.0072)^2$	0.343	-0.141	0.505	-0.1123	0.8600	179.5792	0.201	0.223	0.175
Indoor (*B*) + 1 vertical GCP	$(0.0027)^2$	-0.039	-0.110	1.146	-0.1225	0.8418	179.5522	0.078	0.096	0.121
Indoor (*B*) + 37 vertical GCP	$(0.0026)^2$	-0.033	-0.128	1.123	-0.1186	0.8454	179.5511	0.085	0.099	NA
Indoor (*B*) + 37 full GCP	$(0.0026)^2$	-0.007	-0.144	1.232	-0.1203	0.8436	179.5449	NA	NA	NA
Indoor (*C*) + 1 vertical GCP	$(0.0033)^2$	0.301	-1.546	1.185	-0.0723	0.7977	179.5438	0.082	0.356	0.189
CCC (*B*) + 1 vertical GCP	$(0.0028)^2$	-0.121	-0.465	1.096	-0.1224	0.8433	179.5528	0.095	0.121	0.122
Physically measured values	-	-0.180	-0.170	1.065	-	-	-			

CONCLUSIONS AND RECOMMENDATIONS FOR FUTURE WORK

This paper has investigated the impact of the camera and system mounting parameters calibration on photogrammetric reconstruction. First, a methodology for testing the adequacy of the distortion models and the equivalency of the calibration techniques/datasets was outlined. Then, the aspects involved in the design and implementation of an in-flight mounting parameters calibration, as they relate to control and flight configuration requirements were investigated through mathematical analysis of the GPS/INS assisted camera point-positioning equation. This analysis has led to the optimum flight configuration for the estimation of biases in the system mounting parameters. The devised optimal flight configuration consists of two strips which are captured in opposite directions with as much side lap as possible and two flight lines flown in the same direction with the least side lap possible (30-50%). The presented analysis has also shown that all mounting parameters can be estimated without ground control except the vertical lever-arm parameter that requires one vertical ground control point.

The experimental results section demonstrated that differently from what is usually presumed for MFDCs, K_1 is not sufficient to model the lens distortion of the MFDC used in this research work. Instead, the distortion model including the parameters K_1, K_2 is the adequate model to represent the IOP of the involved camera. Also, it was verified that the indoor calibration provides reliable estimate of the internal camera characteristics and leads to accurate system calibration and object space reconstruction. The adequacy of the distortion model including the parameters K_1, K_2 and the equivalency of the calibration datasets has been tested through the analysis of the outcome of the bundle adjustment with self calibration and bundle similarity methods. In addition, the impact of the calibration techniques and the distortion model on the system mounting parameters estimation and the object space reconstruction under different georeferencing scenarios was investigated. It was proven that a single vertical GCP is sufficient for the estimation of the mounting parameters given that an appropriate flight configuration is used.

Future work will focus on performing more tests with other datasets including imagery suitable for in-situ calibration. Also, it will be verified if the degradation in the obtained results from the GPS/INS with ±10cm and ±10sec accuracy is caused by having a multi-date flights. Moreover, the achievable accuracy from the implemented camera using the estimated mounting parameters in a direct georeferencing procedure will be investigated.

ACKNOWLEDGEMENT

This work was supported by the Canadian GEOIDE NCE Network (SII-72) and the National Science and Engineering Council of Canada (Discovery Grant). The authors would like to thank McElhanney Consulting Services Ltd, BC, Canada for providing the image datasets. Also, the authors are indebted to Mr. Dan Tresa, McElhanney Consulting Services Ltd, for the valuable feedback.

REFERENCES

Brown, D., 1966. Decentric distortion of lenses, *Journal of Photogrammetric Engineering & Remote Sensing*, 32 (3): 444-462.

Brown, D., 1971. Close range camera calibration, *Journal of Photogrammetric Engineering & Remote Sensing*, 37 (8): 855-866.

Cramer, M., 2004. EUROSDR Network on digital camera calibration, *In.: In: International Archives of Photogrammetry and Remote Sensing, XXth ISPRS Congress*, Istanbul, 35 (B3): 210-215.

Ebner, H., 1976. Self-calibrating block adjustment, *Congress of the International Society for Photogrammetry*, Invited Paper of Commission III, Helsinki, Finland.

Grejner-Brzezinska, D. A., 1999. Direct Exterior Orientation of Airborne Imagery with GPS/INS System: Performance Analysis, *Navigation*, 46(4): 261-270.

Grün, A., 1978. Accuracy, reliability and statistics in close-range photogrammetry, *Inter-congress symposium, International Society for Photogrammetry*, Commission V, Stockholm, Sweden.

Habib A., and T. Schenk, 2001. Accuracy Analysis of Reconstructed Points in Object Space from Direct and Indirect Exterior Orienation Methods, *OEEPE Workshop on Integrated Sensor Orientation*. Institute for Photogrammetry and Engineering Surveying, University of Hannover, 17-18 September, 2001.

Habib, A., A. Jarvis, I. Detchev, G. Stensaas, D. Moe, and J. Christopherson, 2008. Standards and specifications for the calibration and stability of amateur digital cameras for close-range mapping applications, *The International Archives of Photogrammetry, Remote Sensing and Spatial Information Sciences – ISPRS Congress Beijing 2008*, 37 (B1): 1059-1064.

Habib, A., A. Pullivelli, E. Mitishita, M. Ghanma, and E. Kim, 2006. Stability analysis of low-cost digital cameras for aerial mapping using different georeferencing techniques, *The Photogrammetric Record*, 21 (113): 29-43.

Jacobsen, K., 2003. Issues and Method for In-Flight and On-Orbit Calibration, *Workshop on Radiometric and Geometric Calibration*, Gulfport, 11 pages.

Jacobsen, K., 2004. Direct/ Integrated Sensor Orientation – Pros and Cons, *The International Archives of Photogrammetry and Remote Sensing,* 35 (B3): 829-835.

Pinto L., G. Forlani, 2002. A single step calibration procedure for IMU/GPS in aerial photogrammetry, *In: International Archives of Photogrammetry and Remote Sensing*, 34 (B3): 210-213.

Skaloud, J., 1999. Optimizing Georeferencing of Airborne Survey Systems by INS/DGPS, Phd Dissertation, Department of Geomatics Engineering, University of Calgary.

USGS, 2008. Procedure for compensation of aerial camera lens distortion as computed by the simultaneous multiframe analytical calibration (SMAC) systems. http://calval.cr.usgs.gov/_osl/smaccompen.pdf (accessed 9 Dec. 2009).